Electronic Supplementary Material (ESI) for Energy & Environmental Science.

Supplementary Information

Optimizing Nanoparticle Perovskite for Bifunctional Oxygen Electrocatalysis

Jae-Il Jung[1], Marcel Risch[2], Seungkyu Park[1], Min Gyu Kim[3], Gyutae Nam[1], Hu-Young Jeong[4],
Yang Shao-Horn*[2] and Jaephil Cho*[1]

[1]School of Energy and Chemical Engineering, Ulsan National Institute of Science & Technology (UNIST)
Ulsan 689–798, Korea

[2]Electrochemical Energy Laboratory, Massachusetts Institute of Technology, 77 Massachusetts Ave.,
Cambridge, MA, 02139, USA

[3]Beamline Research Division, Pohang Accelerator Laboratory, Pohang University of Science and Technology,
Pohang 790-784, South Korea

[4]UNIST Central Research Facilities (UCRF), Ulsan National Institute of Science & Technology (UNIST)
Ulsan 689-798, Korea

Supplementary Figures

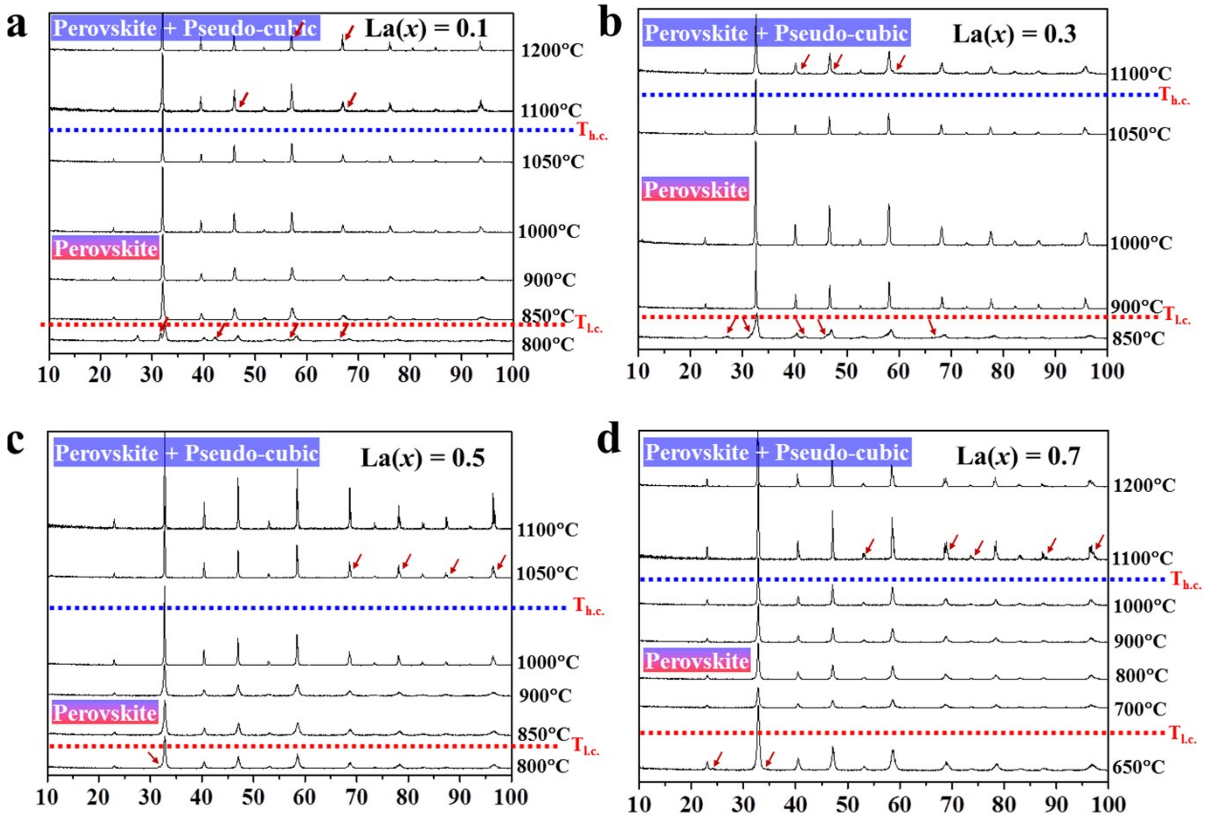

Figure S1. X-ray diffraction patterns of a) La(x) = 0.1, b) La(x) = 0.3, c) La(x) = 0.5 and d) La(x) = 0.7 in $La_x(Ba_{0.5}Sr_{0.5})_{1-x}Co_{0.8}Fe_{0.2}O_{3-\delta}$ calcined for 5h at different calcination temperatures (°C), where pure cubic perovskite phase exist between the lower critical temperature ($T_{l.c.}$) and the higher critical temperature ($T_{h.c.}$). The perovskite phase emerges above the lower critical temperatures ($T_{l.c.}$). The overall defects are supposed to maintain the electroneutrality condition on the assumption that defects are single, unassociated and randomly distributed within dilute solution (Equation S2). However, in reality, while the ideal model is generally applicable in a solution with lower defect concentration than 1%, new defect structure situations are expected to form defect complexes or microdomains of ordered defects, where the critical driving forces such as charge imbalance and the preferential increase of crystallinity around Co-site sub-lattice can cause structural stress on the cubic perovskite, in accordance as A-site cations are replaced with La^{3+} cations. Above the higher critical temperature ($T_{h.c.}$) cubic perovskite and psedo-perovskite phases begin to coexist. The tendency of forming such defect complexes according to temperature changes can be expressed in the mass-action of equation S3. Since the complexes break below the critical temperatures, the corresponding formation enthalpy, ΔH, can be considered as positive in this study, signifying that it is an endothermic reaction.

$$La_2O_3 \xrightarrow{AO} 2La_A^{\bullet} + 2O_O + \frac{1}{2}O_2(g) + 2e' \tag{S1}$$

$$\left[B_B^{/}\right] = \left[La_A^{\bullet}\right] + 2\left[V_O^{\bullet\bullet}\right] \tag{S2}$$

$$\frac{\left[\left(La_A^{\bullet} \cdot Co_B^{/}\right)\right]}{\left[La_A^{\bullet}\right]\left[Co_B^{/}\right]} = K(T) = K^o e^{-\Delta H / kT} e^{\Delta S / k} \tag{S3}$$

where $La_A^{\bullet}$ denotes the substitution of La^{3+} for A^{2+} in the A-site cation, $V_O^{\bullet\bullet}$ denotes an oxygen anion vacancy and $B_B^{/}$ denotes the substitution of the lower valance of B^{3+}/B^{2+} for the higher valence of B^{4+}/B^{3+}, respectively, in the B-site cation.

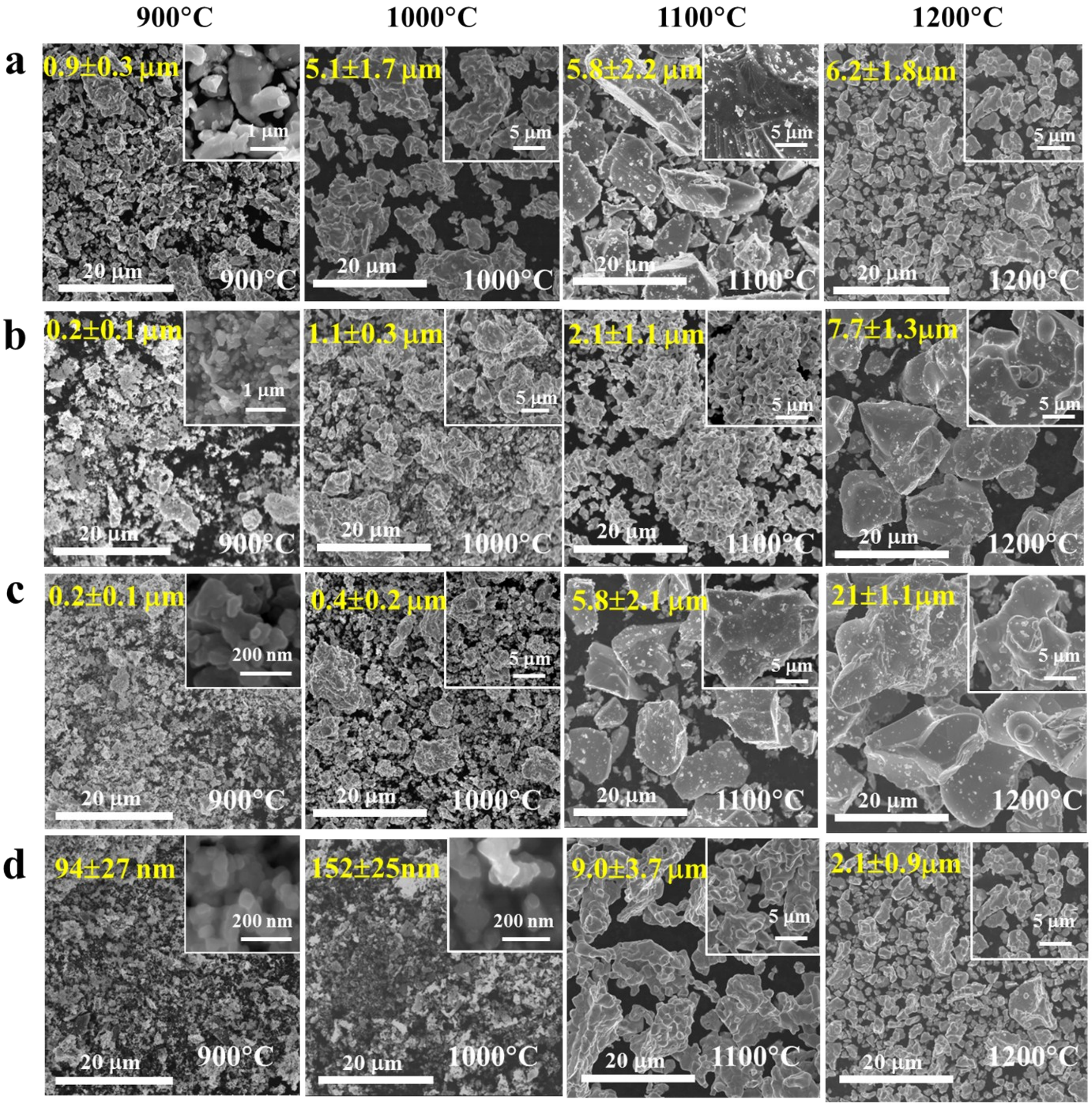

Figure S2. SEM images of a) La(x) = 0.1, b) La(x) = 0.3, c) La(x) = 0.5 and d) La(x) = 0.7 in $La_x(Ba_{0.5}Sr_{0.5})_{1-x}Co_{0.8}Fe_{0.2}O_{3-\delta}$ calcined at 900 °C, 1000 °C, 1100 °C and 1200 °C for 5h.

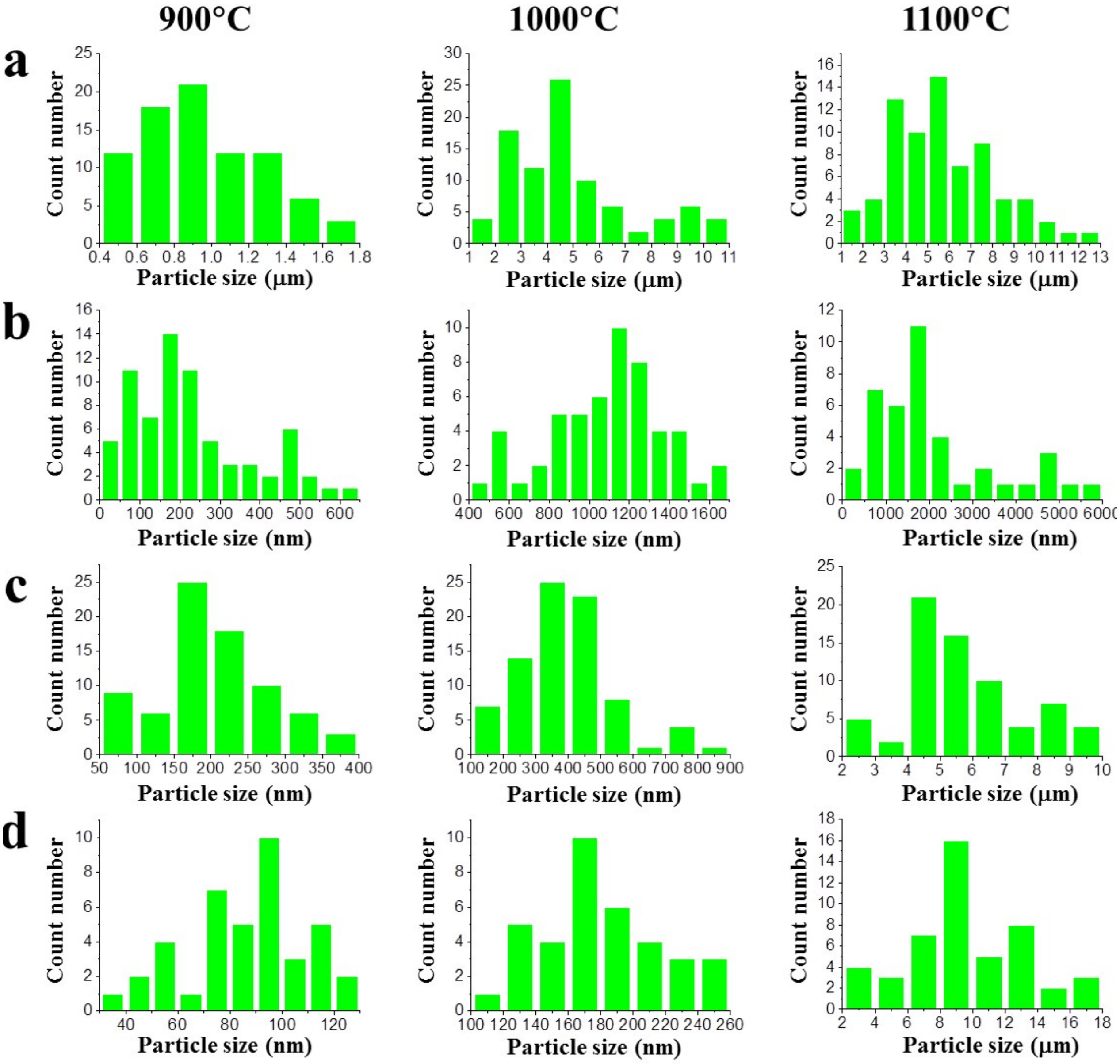

Figure S3. Histograms of particle size distribution for a) La(x) = 0.1, b) La(x) = 0.3, c) La(x) = 0.5 and d) La(x) = 0.7 in $La_x(Ba_{0.5}Sr_{0.5})_{1-x}Co_{0.8}Fe_{0.2}O_{3-\delta}$ calcined at 900 °C, 1000 °C and 1100 °C for 5h.

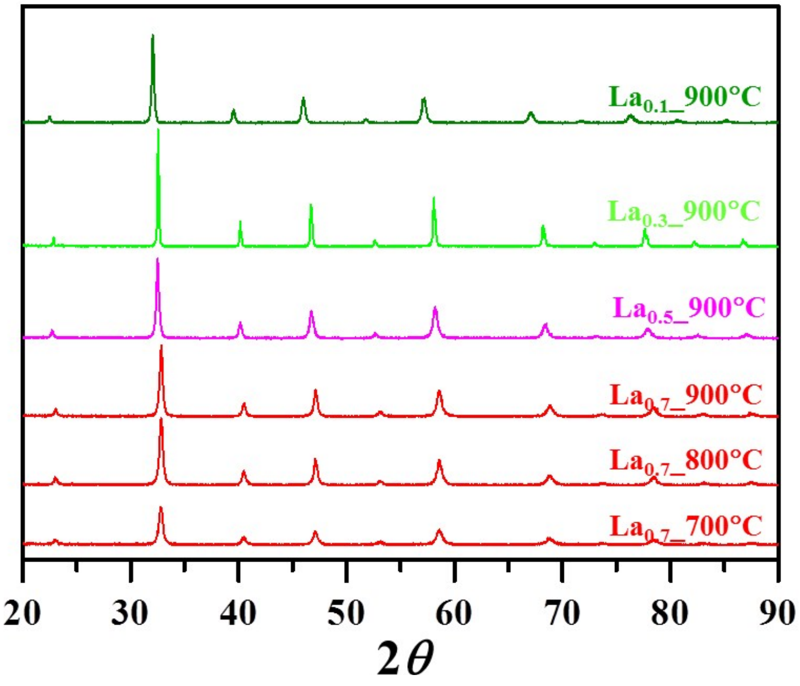

$La_{0.7}$	Crystallite size (nm) According to Sherrer Eq.
900°C	69.9 ± 26.8
850°C	55.6 ± 20.2
800°C	40.5 ± 27.8
750°C	36.4 ± 22.6
700°C	35.8 ± 14.6

Figure S4. Crystallite size growth of La(x) = 0.7 in $La_x(Ba_{0.5}Sr_{0.5})_{1-x}Co_{0.8}Fe_{0.2}O_{3-\delta}$ .vs calcination temperature according to Scherrer equation from X-ray diffraction patterns.

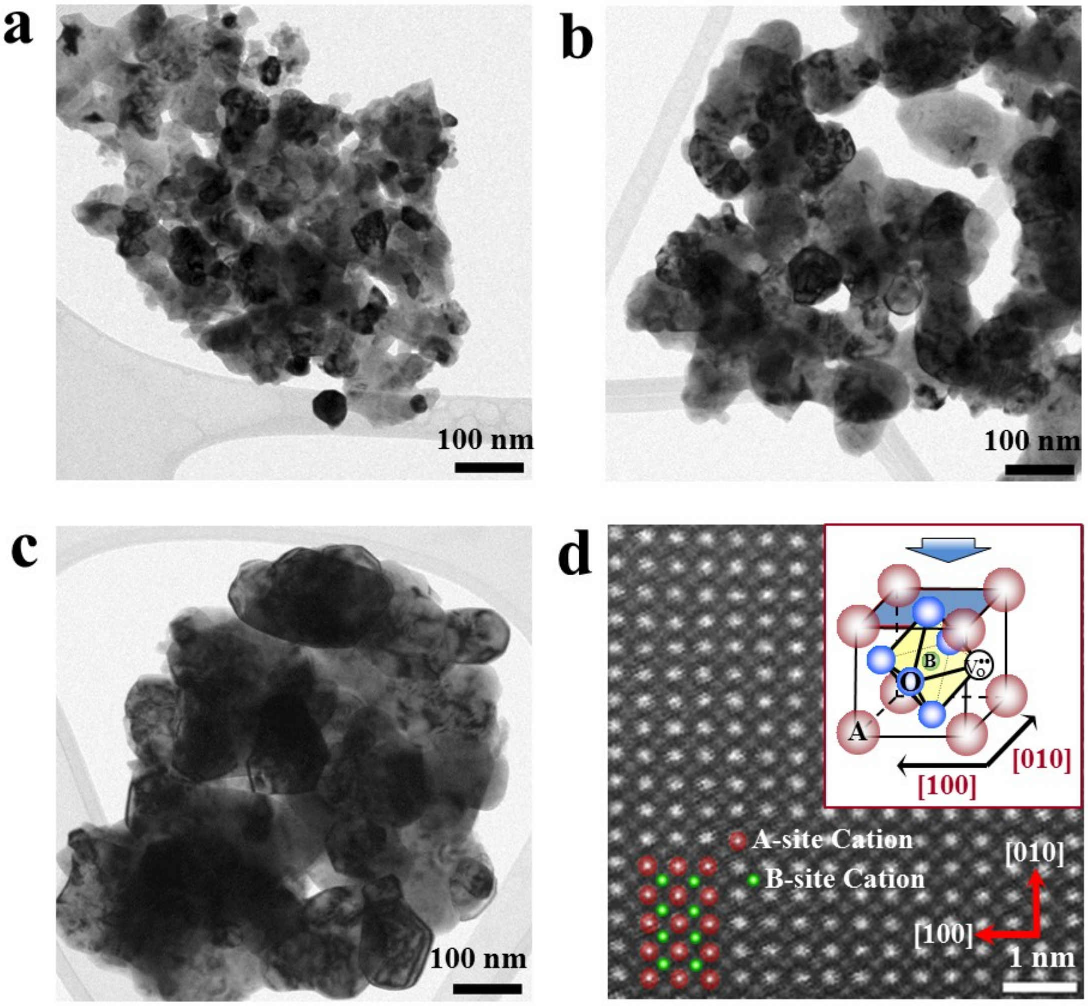

Figure S5. BFTEM images of a) La0.7-50nm (700℃), b) La0.7-70nm (800℃), c) La0.7-100nm (900℃), and d) HAADF STEM image showing the atomic arrangements of cubic perovskite structure

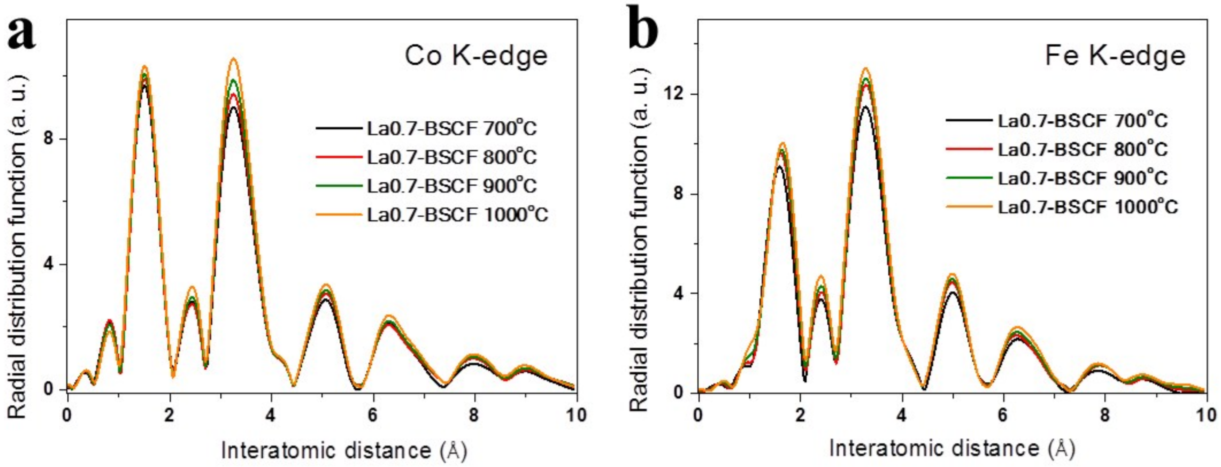

Figure S6. Radial distribution function of a) Co and b) Fe of *K*-edge XAFS x = 0.7 in $La_x(Ba_{0.5}Sr_{0.5})_{1-x}Co_{0.8}Fe_{0.2}O_{3-\delta}$ .vs calcination temperature.

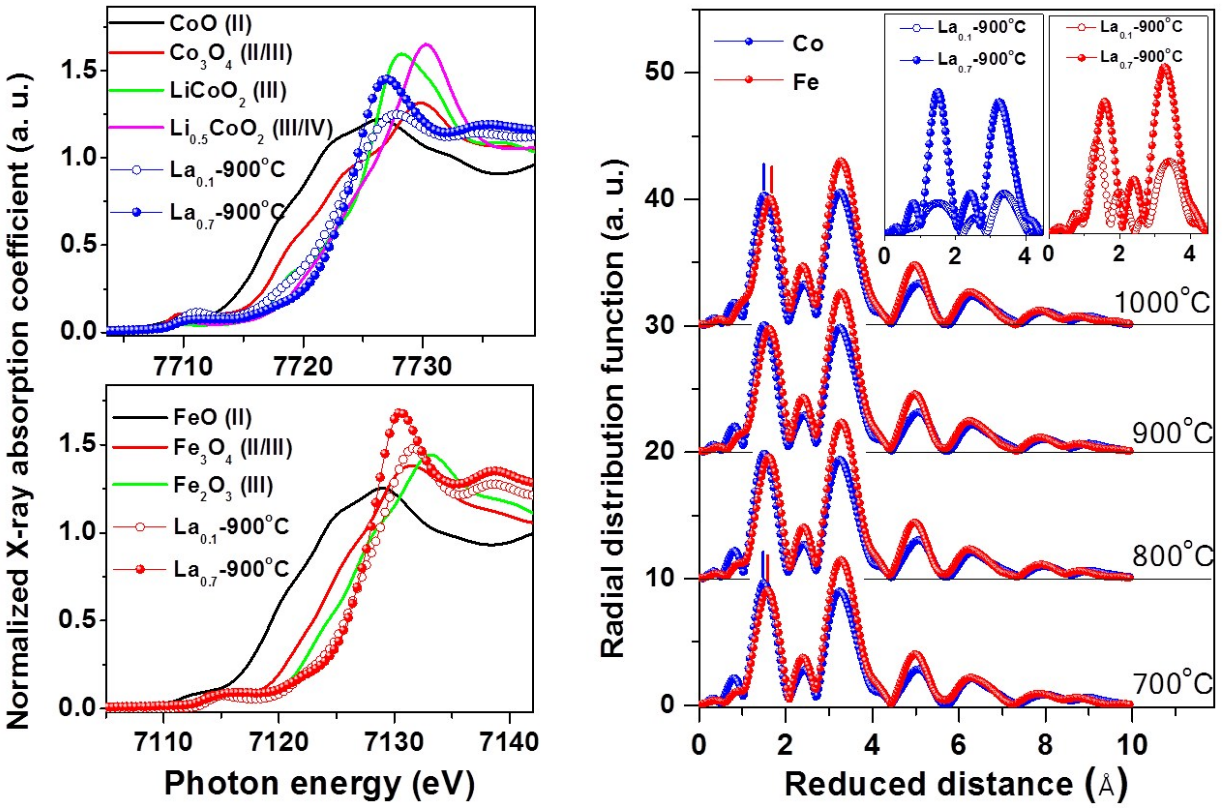

Figure S7. a) Normalized Co and Fe K-edge XANES spectra for $La_{0.7\_900°C}$ ($La_{0.7}$-100nm) (blue filled circle) and $La_{0.1\_900°C}$ ($La_{0.1}$-1µm) (blue empty circle) and references, and **b**) RDFs of Fourier-transformed k^3-weighted EXAFS spectra for $La_{0.7\_700°C}$ ($La_{0.7}$-50nm), $La_{0.7\_800°C}$($La_{0.7}$-70nm), $La_{0.7\_900°C}$ ($La_{0.7}$-100nm) and $La_{0.7\_1000°C}$. The inset shows that, as La concentration decreases, the crystallinity of Co octahedron sub-lattice decreases significantly, and the bond length between Fe-O decreases.

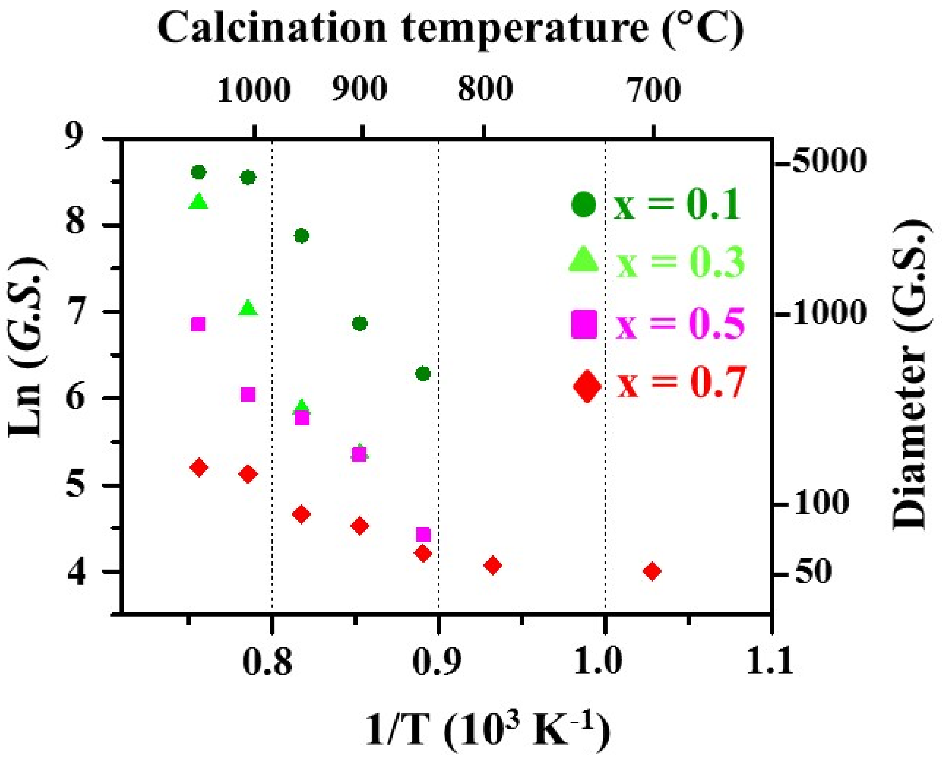

Figure S8. Arrhenius plot of Ln (G.S.) (G.S. denotes the grain size of each particle) as a function of 1/T ($10^3 K^{-1}$) for La(x) = 0.1 (green circles), b) La(x) = 0.3 (light green triangles), c) La(x) = 0.5 (pink square) and d) La(x) = 0.7 (red diamonds) in $La_x(Ba_{0.5}Sr_{0.5})_{1-x}Co_{0.8}Fe_{0.2}O_{3-\delta}$.

When the particle size growth rate vs. calcination temperature (dG/dT) of Figure 1 is replotted into Ln (G) vs 1/T (10^3 K^{-1}) (Figure S9), the corresponding activation energies (Q) according to the increasing La(x) can be obtained according to the general Arrhenius equation as described in equation (S4).

$$G - G_o = kt \qquad \text{(S4)}$$

$$= tk_O \exp\left(-\frac{Q}{KT}\right)$$

where, Boltzmaan constant K is 8.62 ×10^{-5} eV/atom-K. With increasing x, the activation energy (Q) increases from 1.64 eV/atom at La(x) = 0.1 to 2.60 eV/atom-K at La(x) = 0.3 as an apex, from which the activation energy begins decreases up to Q = 0.34 eV/atom-K at La(x) = 0.7.

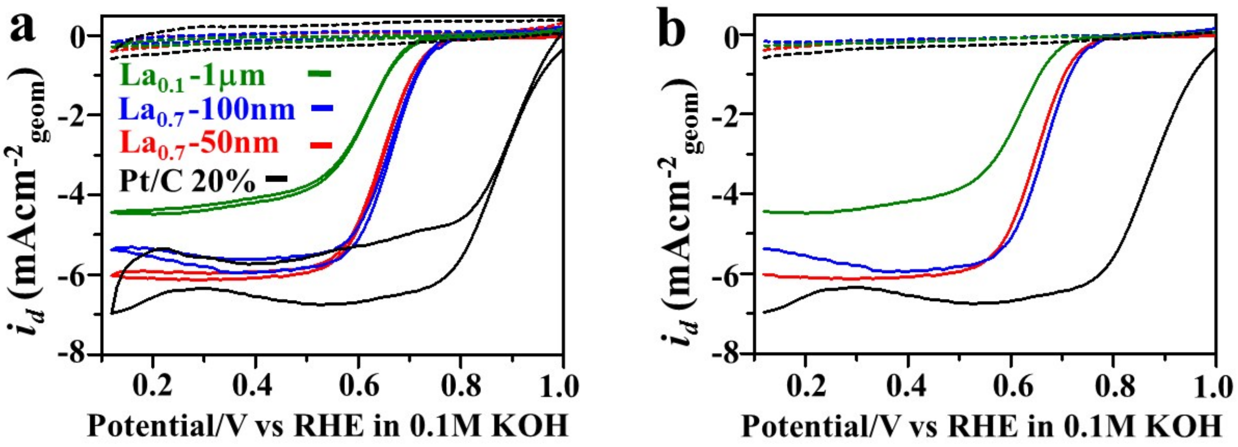

Figure S9. ORR activities of $La_{0.1}(Ba_{0.5}Sr_{0.5})_{0.9}Co_{0.8}Fe_{0.2}O_{3-\delta}$ ($La_{0.1}$-1μm)(green), $La_{0.7}(Ba_{0.5}Sr_{0.5})_{0.3}Co_{0.8}Fe_{0.2}O_{3-\delta}$-100nm ($La_{0.7}$-100nm)(blue) and $La_{0.7}(Ba_{0.5}Sr_{0.5})_{0.3}Co_{0.8}Fe_{0.2}O_{3-\delta}$-50nm ($La_{0.7}$-50nm)(red) and Pt/C 20wt% (black) as a function of potential on GCE in oxygen saturated 0.1 M KOH electrolyte at 10 mVs^{-1} scan rate at 1600 rpm under the saturated oxygen gas (line) and under the saturated argon gas (dot) by a) scanning forward and backward (positive and negative-going) and b) scanning forward .

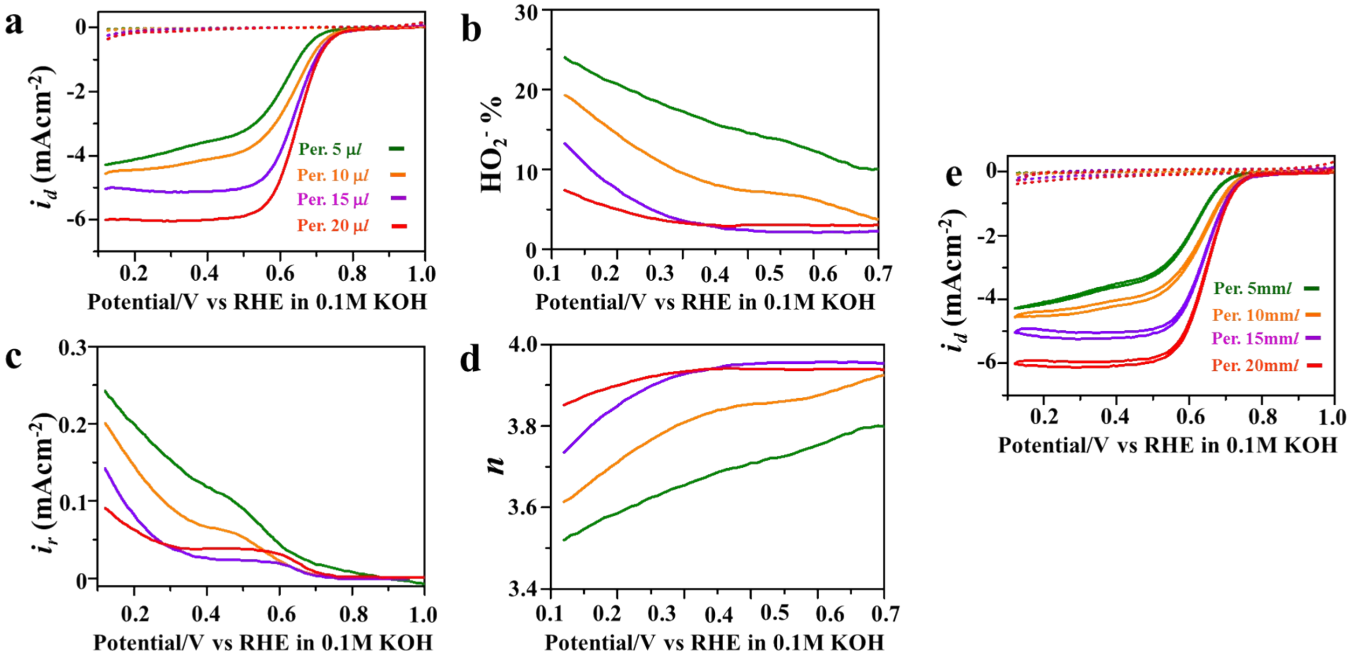

Figure S10. ORR (capacitance-corrected) of $La_{0.7}(Ba_{0.5}Sr_{0.5})_{0.3}Co_{0.8}Fe_{0.2}O_{3-\delta}$-50nm ($La_{0.7}$-50nm) according to the increasing portion of perovskite catalysts (5 μ*l* (green), 10 μ*l* (orange), 15 μ*l* (violet) and 20 μ*l* (red line) of $La_{0.7}$-50nm). a) disc and c) ring currents (Voltammograms) of the ORR and the determined b) peroxide percentage (HO_2^- %) and d) electron transfer number (n) using RRDEs at 1600 rpm and the scan rate of 10 mVs^{-1} in 0.1M KOH under the saturated oxygen gas (line) and under the saturated argon gas (dot), where e) as-measured ORR activities of the composite catalyst) are capacity-corrected by taking an average of forward and backward (positive and negative-going) scans. The all oxide electrode composites of 5 μ*l* (green), 10 μ*l* (orange), 15 μ*l* (pink) and 20 μ*l* (red) contain (0.16, 0.32, 0.48 and 0.64) mg_{ox}/cm^2_{disk}, (0.04, 0.08, 0.12 and 0.16) mg_{KB}/cm^2_{disk}, 0.35 mg_{Nafion}/cm^2_{disk}, respectively.

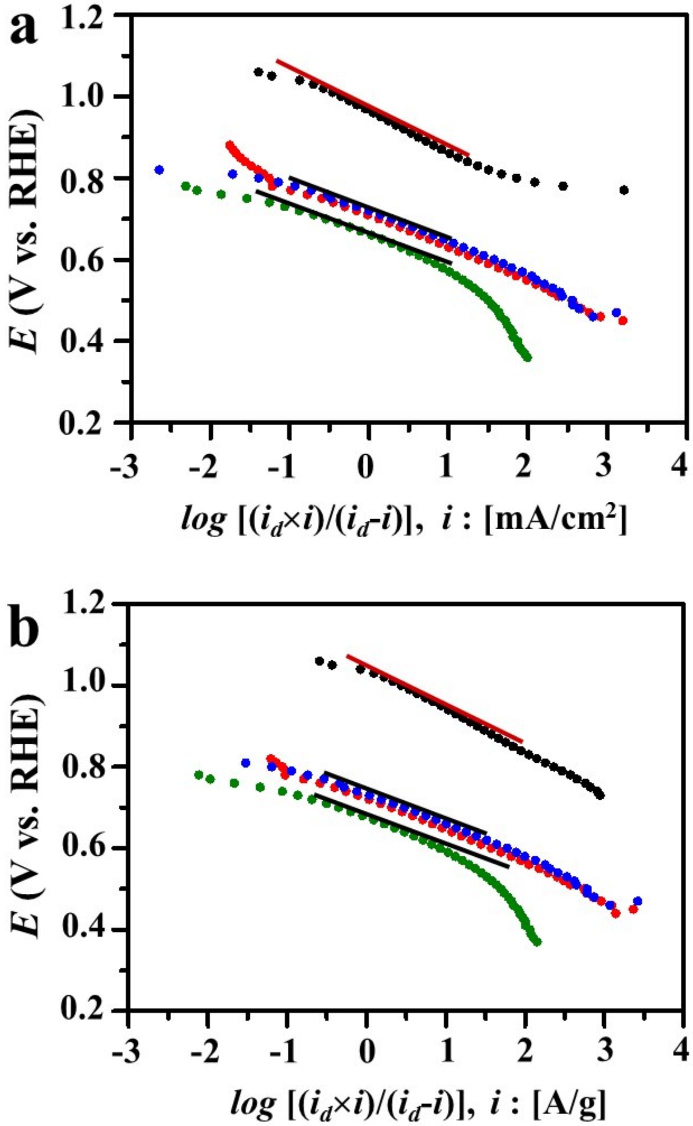

	Tafel slope (mV/dec)
La$_{0.1}$-1μm	**77**
La$_{0.7}$-100nm	**72**
La$_{0.7}$-50nm	**71**
Pt 20%	**99**

	Tafel slope (mV/dec)
La$_{0.1}$-1μm	**79**
La$_{0.7}$-100nm	**72**
La$_{0.7}$-50nm	**73**
Pt 20%	**98**

Figure S11. Tafel plots of the a) geometric ORR activities (*i* : [mA/cm^2]) and b) mass ORR activities (*i* : [A/g]) for La$_{0.1}$(Ba$_{0.5}$Sr$_{0.5}$)$_{0.9}$Co$_{0.8}$Fe$_{0.2}$O$_{3-\delta}$ (La$_{0.1}$-1μm)(green line), La$_{0.7}$(Ba$_{0.5}$Sr$_{0.5}$)$_{0.3}$Co$_{0.8}$Fe$_{0.2}$O$_{3-\delta}$-100nm (La$_{0.7}$-100nm)(blue line) and La$_{0.7}$(Ba$_{0.5}$Sr$_{0.5}$)$_{0.3}$Co$_{0.8}$Fe$_{0.2}$O$_{3-\delta}$-50nm (La$_{0.7}$-50nm)(red line) and Pt/C 20% (black line) as a function of potential on GCE in oxygen saturated 0.1M KOH electrolyte at 10 mVs^{-1} scan rate at 1600 rpm, and the corresponding Tafel slopes where ORR activities initiate.

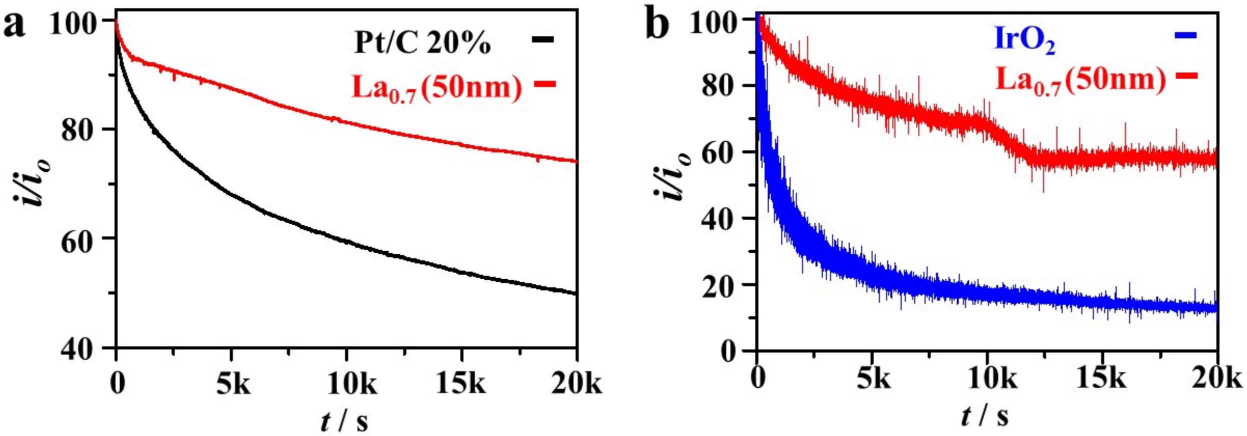

Figure S12. Electrocatalytic properties (chronoamperometric method) of a relative (i/i_o) currents using RDEs at 1600 rpm and a) 0.7 V (vs RHE) for ORR and b) 1.5 V (vs RHE) for OER in 0.1M KOH under the saturated oxygen gas. 20% Pt on Vulcan XC-72 (E-tek) (black line), $La_{0.7}$(50nm) (red line) and IrO_2 (blue line).

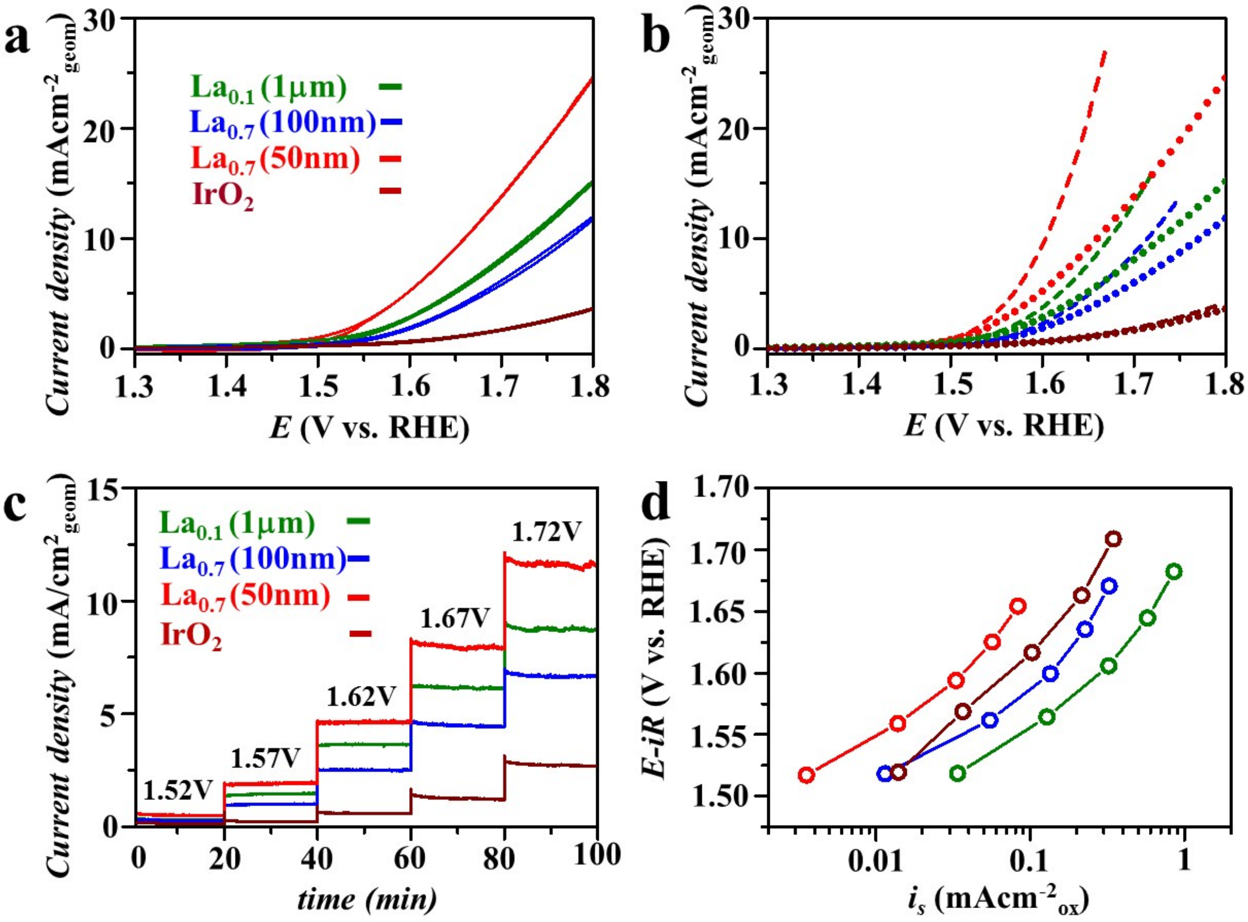

Figure S13. Ohmic and capacitive corrections of the as-measured OER activities for perovskite oxide catalysts. a) The as-measured OER activities of $La_{0.1}(Ba_{0.5}Sr_{0.5})_{0.9}Co_{0.8}Fe_{0.2}O_{3-\delta}$ ($La_{0.1}$-1μm)(green line), $La_{0.7}(Ba_{0.5}Sr_{0.5})_{0.3}Co_{0.8}Fe_{0.2}O_{3-\delta}$-100nm ($La_{0.7}$-100nm)(blue line) and $La_{0.7}(Ba_{0.5}Sr_{0.5})_{0.3}Co_{0.8}Fe_{0.2}O_{3-\delta}$-50nm ($La_{0.7}$-50nm)(red line) and IrO_2 (brown line) as a function of potential on GCE in oxygen saturated 0.1M KOH electrolyte at 10 mVs^{-1} scan rate at 1600 rpm is capacity-corrected by taking an average of forward and backward (positive and negative-going) scans. b) The capacity-corrected OER currents (dot line) are then ohmically corrected with the measured ionic resistance (≈45 Ω) to yield the final electrode OER activity (long-dash line). (c) OER currents at select potentials, and d) Tafel plot of specific OER activities normalized to the catalyst surface area (listed in Table S2).

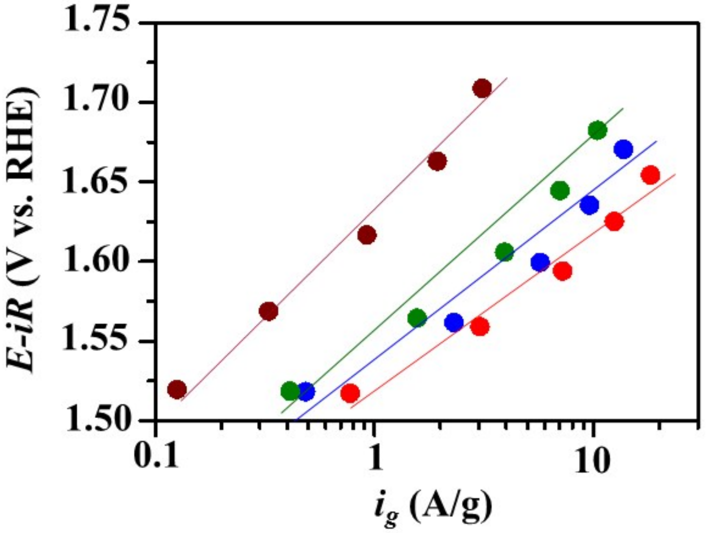

	Tafel slope (mV/dec)
$La_{0.1}$-1μm	**112**
$La_{0.7}$-100nm	**99**
$La_{0.7}$-50nm	**97**
IrO_2	**130**

Figure S14. Tafel plot of the OER specific activities of $La_{0.1}(Ba_{0.5}Sr_{0.5})_{0.9}Co_{0.8}Fe_{0.2}O_{3-\delta}$ ($La_{0.1}$-1μm)(green line), $La_{0.7}(Ba_{0.5}Sr_{0.5})_{0.3}Co_{0.8}Fe_{0.2}O_{3-\delta}$-100nm ($La_{0.7}$-100nm)(blue line) and La $_{0.7}(Ba_{0.5}Sr_{0.5})_{0.3}Co_{0.8}Fe_{0.2}O_{3-\delta}$-50nm ($La_{0.7}$-50nm)(red line) and RuO_2 (brown line) as a function of potential on GCE in oxygen saturated 0.1M KOH electrolyte at 10 mVs^{-1} scan rate at 1600 rpm. All the activities are iR-corrected, and the gravimetric OER activities in Tafel plot are normalized to the applied catalyst weight (0.08 mg). At least three independent measurements were executed in order to confirm the repeatability of the experimental results for each sample.

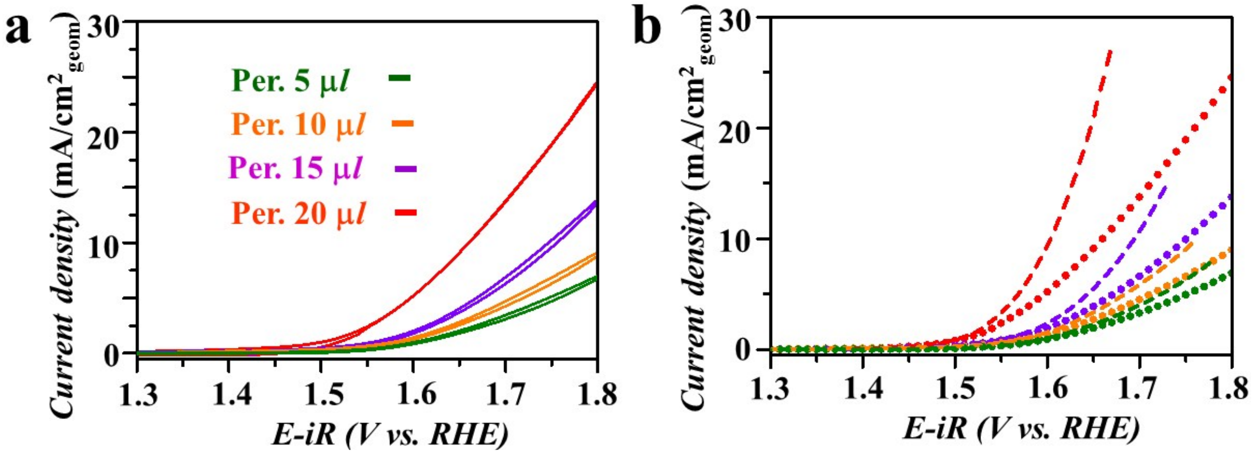

Figure S15. Ohmic and capacitive corrections of the as-measured OER activities for perovskite oxide catalysts. a) The as-measured OER activities of La$_{0.7}$(Ba$_{0.5}$Sr$_{0.5}$)$_{0.3}$Co$_{0.8}$Fe$_{0.2}$O$_{3-\delta}$-50nm (La$_{0.7}$-50nm) according to the increasing portion of perovskite catalysts (5 μ*l*(green), 10 μ*l* (orange), 15 μ*l* (violet line) and 20 μ*l* (red line) of La$_{0.7}$-50nm) as a function of potential on GCE in oxygen saturated 0.1M KOH electrolyte at 10 mVs^{-1} scan rate at 1600 rpm is capacity-corrected by taking an average of forward and backward (positive and negative-going) scans. b) The capacity-corrected OER currents (dot line) are then ohmically corrected with the measured ionic resistance (≈45 Ω) to yield the final electrode OER activity (long-dash line). The all oxide electrode composites of 5 μ*l* (green line), 10 μ*l* (orange), 15 μ*l* (pink line) and 20 μ*l* contain (0.16, 0.32, 0.48 and 0.64) mg$_{ox}$/cm$^2_{disk}$, (0.04, 0.08, 0.12 and 0.16) mg$_{KB}$/cm$^2_{disk}$, 0.35 mg$_{Nafion}$/cm$^2_{disk}$, respectively.

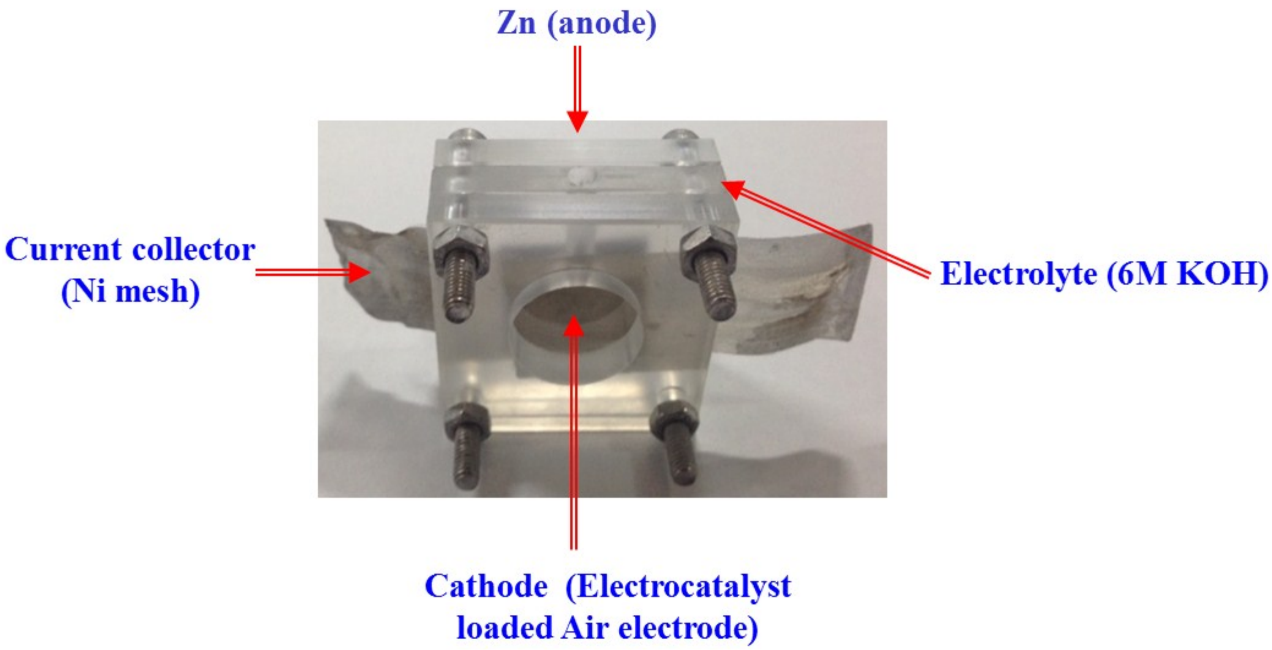

Figure S16. The full-cell is structured with 0.8g Zn foil as anode, 6 M KOH electrolyte, Ni mesh as current collector and air cell. Air electrode was fabricated with 60% of active carbon, 5% of catalyst, 3% of KB as conductor and 32% of PTFE binder. A separator was not applied because the electrode distance was sufficiently large.

.

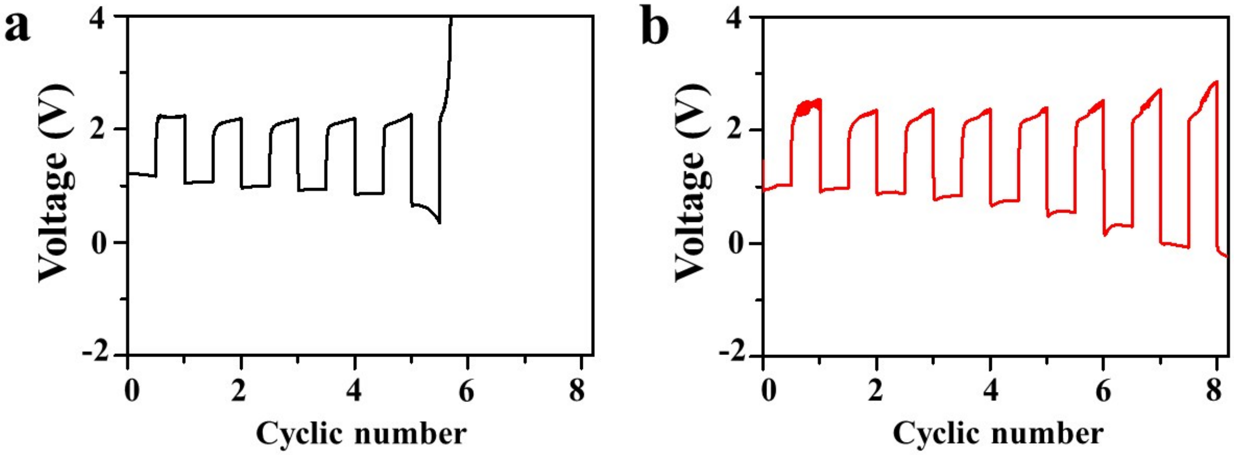

Figure S17. The repeated charge and discharge test as Zn-air full-cell under 10.5 mAcm^{-2} in 6 M KOH with **(a)** Pt/C 20% and **(b)** La$_{0.7}$-50nm catalyst as long time cycle, where 1 cycle consists of the 3600 s of discharge, followed by 3600 s of charge flows. Increased degradation as compared to Figure 4 in the main text is likely due to anode and carbon corrosion rather than catalyst degradation.

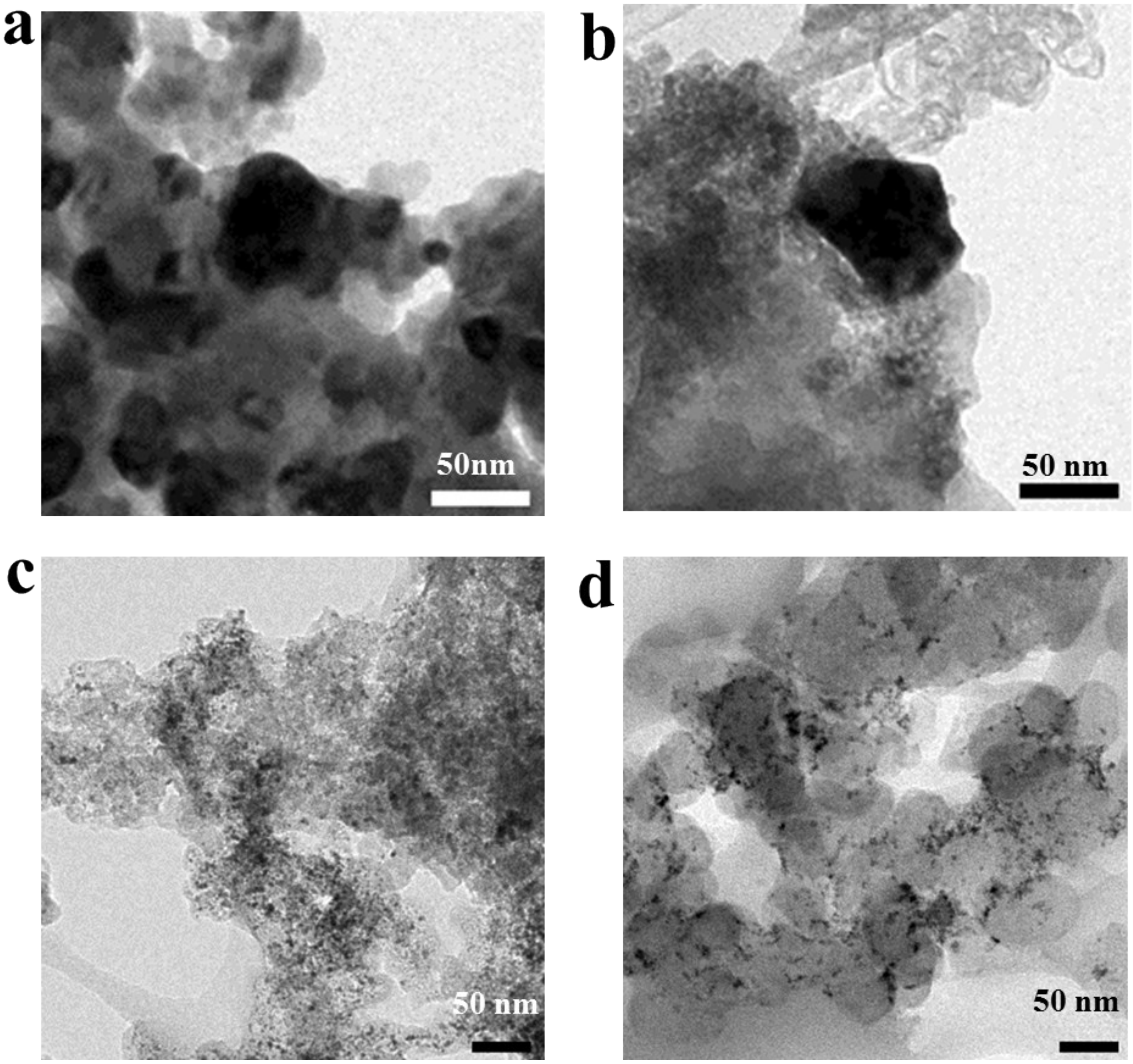

Figure S18. BFTEM images on the surfaces of $La_{0.7}(Ba_{0.5}Sr_{0.5})_{0.3}Co_{0.8}Fe_{0.2}O_{3-\delta}$ ($La_{0.7}$-50nm) particles **a**) before and **b**) after 100th cycle and Pt/C 20% particles **c**) before and **d**) after 100th cycle of the short time full-cell tests.

Table S1. EXAFS Structural parameters of Fe and Co Kedge k^3-weighted EXAFS spectra for La-doped $[Ba_{0.5}Sr_{0.5}][Co_{0.8}Fe_{0.2}]O_{3-\delta}$ samples.

	Edge	Path	Energy shift (eV)	CN number	Interatomic distance (Å)	Debye-Waller factor (Å^{-2})

700^{o}C	Fe K-edge	Fe - O	0.4	4.68	1.99(3)	1.39
		Fe – Fe/Co*	9.6	0.92	2.74(1)	7.20
		Fe – La/Ba/Sr	-5.7	8.00	3.53(7)	5.38
		Fe – Fe/Co	-11.8	5.52	3.95(8)	2.81
	Co K-edge	Co - O	-1.6	5.88	1.91(2)	3.08
		Co – Fe/Co*	0.5	2.04	3.06(4)	12.30
		Co – La/Ba/Sr	0.1	7.68	3.52(8)	5.89
		Co – Fe/Co	-10.6	5.52	3.90(7)	6.32
800^{o}C	Fe K-edge	Fe - O	3.5	4.86	2.00(7)	1.35
		Fe – Fe/Co*	9.6	0.92	2.74(1)	7.20
		Fe – La/Ba/Sr	-5.9	8.00	3.53(5)	5.13
		Fe – Fe/Co	-12.1	5.64	3.95(9)	2.33
	Co K-edge	Co - O	-1.8	5.88	1.91(3)	2.95
		Co – Fe/Co*	0.5	2.04	3.06(4)	12.30
		Co – La/Ba/Sr	-0.3	7.84	3.52(4)	5.86
		Co – Fe/Co	-11.2	5.70	3.90(3)	6.25
900^{o}C	Fe K-edge	Fe - O	4.9	4.92	2.01(3)	1.32
		Fe – Fe/Co*	9.6	4.00	3.06(4)	7.20
		Fe – La/Ba/Sr	-5.8	7.68	3.53(4)	4.84
		Fe – Fe/Co	-12.0	1.38	3.96(1)	2.34
	Co K-edge	Co - O	-1.8	5.88	1.91(3)	2.788
		Co – Fe/Co*	0.5	2.04	3.06(4)	12.30
		Co – La/Ba/Sr	-0.1	8.00	3.52(6)	5.59
		Co – Fe/Co	-10.7	5.88	3.90(7)	6.41
1000^{o} C	Fe K-edge	Fe - O	6.0	5.04	2.01(9)	1.32
		Fe – Fe/Co*	9.6	0.92	2.74(1)	7.20
		Fe – La/Ba/Sr	-5.6	8.00	3.53(2)	4.82
		Fe – Fe/Co	-12.6	5.82	3.96(4)	2.31
	Co K-edge	Co - O	-1.8	6.00	1.91(3)	2.66
		Co – Fe/Co*	0.5	2.04	3.06(4)	5.14
		Co – La/Ba/Sr	-0.1	8.00	3.52(6)	6.10
		Co – Fe/Co	-10.7	5.88	3.90(9)	12.30

* The scattering path means a trace local environment of Co and Fe site corresponding to an edge-sharing which is originated from a kind defect site in perovskite structure. The calculation of the EXAFS parameters for the path has been minimized in the XAFS curve-fitting process.

Table S2. The values of particle sizes and surface areas (A_s:m^2g^{-1}) for $La_{0.1}$-1μm , $La_{0.7}$-100nm, $La_{0.7}$-50nm and IrO_2. The surface areas were measured by nitrogen Brunauer, Emmett, and Teller (BET) method.

	Particle size	**A_s (m^2g^{-1})**
$La_{0.1}$-1μm (900 °C)	1.0 ± 0.4 μm	1.2
$La_{0.7}$-100nm (900 °C)	92.8 ± 26.2 nm	4.2
$La_{0.7}$-50nm (700 °C)	54.8 ± 30.0 nm	21.9
IrO_2	2.3 ± 0.9 μm	0.9

Table S3. EXAFS Structural parameters of Fe and Co Kedge k^3-weighted EXAFS spectra for 100th cycled La-doped $[Ba_{0.5}Sr_{0.5}][Co_{0.8}Fe_{0.2}]O_{3-\delta}$ $_{(}La_{0.7}$-50nm)samples

	Edge	Path	Energy shift (eV)	CN number	Interatomic distance (Å)	Debye-Waller factor (Å^{-2})
As-prepared at 700^{o}C	Fe K-edge	Fe - O	0.4	4.68	1.99(3)	1.39
		Fe – Fe/Co*	9.6	0.92	2.74(1)	7.20
		Fe – La/Ba/Sr	-5.7	8.00	3.53(7)	5.38
		Fe – Fe/Co	-11.8	5.52	3.95(8)	2.81
	Co K-edge	Co - O	-1.6	5.88	1.91(2)	3.08
		Co – Fe/Co*	0.5	2.04	3.06(4)	12.30
		Co – La/Ba/Sr	0.1	7.68	3.52(8)	5.89
		Co – Fe/Co	-10.6	5.52	3.90(7)	6.32
200th cycled	Fe K-edge	Fe - O	-4.9	4.86	1.97(4)	1.34
		Fe – Fe/Co*	9.6	0.92	2.74(1)	7.20
		Fe – La/Ba/Sr	-7.5	5.36	3.51(9)	4.30
		Fe – Fe/Co	-14.4	3.90	3.94(6)	2.83
	Co K-edge	Co - O	1.8	6.00	1.93(1)	3.08
		Co – Fe/Co*	0.5	2.04	3.06(4)	12.30
		Co – La/Ba/Sr	-2.3	7.36	3.51(2)	5.89
		Co – Fe/Co	-3.8	4.50	3.96(1)	6.32

* The scattering path means a trace local environment of Co and Fe site corresponding to an edge-sharing which is originated from a kind defect site in perovskite structure. The calculation of the EXAFS parameters for the path has been minimized in the XAFS curve-fitting process.

Table S4. ORR and OER half-cell activities 0.1 M O_2-saturated KOH or NaOH.

Electrocatalyst (ORR)	**BET area (m^2/g)**	**Current density (A/g)**	**at potential**
$LaMnO_3$[a]	0.6*	1.6	0.7 V vs. RHE
$La_{0.5}Ca_{0.5}MnO_3$[a]	2.1*	0.5	0.7 V vs. RHE
$LaCoO_3$[a]	0.7*	2.5	0.7 V vs. RHE
BSCF[b]	0.9	1.2	0.7 V vs. RHE
$BaTiO_{3-\delta}$[c]	24.7	2.0	0.7 V vs. RHE
$La_{0.7}$-50nm[d]	21.9	3	0.7 V vs. RHE
Electrocatalyst (OER)	**BET area (m^2/g)**	**Current density (A/g)**	**at potential**
$La_{0.75}Sr_{0.2}Mn_{0.9}Co_{0.1}O_3$[e]	1.6	1.1	1.8 V vs. RHE
$La_{0.6}Sr_{0.4}FeO_3$[e]	1.8	1.6	1.8 V vs. RHE
$La_{0.58}Sr_{0.4}Co_{0.2}Fe_{0.8}O_3$[e]	0.6	3.9	1.8 V vs. RHE
$La_{0.74}Sr_{0.2}Co_{0.2}Fe_{0.8}O_3$[e]	0.7	4.6	1.8 V vs. RHE
$La_{0.83}Ca_{0.15}Mn_{0.6}Co_{0.4}O_3$[e]	0.7	2.2	1.8 V vs. RHE
$LaCoO_3$[f]	0.7*	1.4	1.6 V vs. RHE
$BaTiO_{3-\delta}$[c]	24.7	1.5	1.6 V vs. RHE
$La_{0.7}$-50nm[d]	21.9	8	1.6 V vs. RHE

We caution that the oxide loading and carbon loading/type may affect the activity. Considering these factors, we estimate an experimental uncertainty in the activity of approximately an order of magnitude when comparing work from different laboratories. * from SEM/TEM analysis

a Suntvich et al., *Nat. Chem.* 3, 546 (2011); KOH

b Suntivich et al., *Electrocatal.* 4, 49 (2013); KOH

c Chen et al., *Nano Energy* 13, 423 (2015); KOH

d This work; KOH

e Rincon et al., *ChemPhysChem* 15, 2810 (2014); NaOH

f May et al., J. Phys Chem Lett 3, 3264 (2012); KOH

Table S5. Zn-air full cell performance in literature.

Electrocatalyst	**Current Density(mA/cm^2)**	**Cycle Condition**	**Polarization at the end**
CoO/N-CNT+ NiFe LDH[a]	20~50	4~20h per cycle (oxygen blowing with tri-electrode system)	Negligible V change
CNT/MnO_2[b]	8	600s per cycle periods for 50 cycles	0.4 V
$LaNiO_3$/N-CNT[c]	17.6	600s per cycle periods for 75 cycles	0.1~0.4V
MnO_2/SS[d]	5~15	24h per cycle periods for 120h	Negligible V change
NCNT/CoO-NiO-NiCo[e]	20	600s per cycle periods for 16.5h	0.1V
$La_{0.7}$-50nm[f]	10.5	600s per cycle for 100 cycles	0.05~0.1V

a Yanguang et al., *Nat. Commun*. 4 (2013)

b Zhu et al., *Electrochim. Acta*. 69, 295 (2012)

c Zhu et al., *Nano Lett.* 11, 5362 (2011)

d Toussaint et al., *ECS Trans*. 28, 25 (2011)

e Xien et al., *Angew. Chem. Int. Ed*., (2015)

f This work